THE JOURNAL OF PHYSICAL CHEMISTRY C

pubs.acs.org/JPCC Article

Bismuth Substituted Strontium Cobalt Perovskites for Catalyzing Oxygen Evolution

Denis A. Kuznetsov,[#] Jiayu Peng,[#] Livia Giordano, Yuriy Román-Leshkov, and Yang Shao-Horn*

Cite This: J. Phys. Chem. C 2020, 124, 6562−6570 Read Online

ABSTRACT: In this study, we employ the concept of inductive effect through substitution with more electronegative/Lewis acidic A-site ions in the cobalt perovskites to alter the O 2p band center and surface hydroxide affinity to promote oxygen evolution reaction (OER) activity and high stability in the basic electrolyte. Galvanostatically charged (fully oxidized, $\delta \approx 0$) $Bi_{0.2}Sr_{0.8}CoO_{3-\delta}$ was shown to exhibit record OER specific activity exceeding not only $La_xSr_{1-x}CoO_{3-\delta}$ but also oxidized $SrCoO_{3-\delta}$, one of the most active oxide OER catalysts reported so far. The enhanced OER kinetics of the oxidized $Bi_{0.2}Sr_{0.8}CoO_{3-\delta}$ is attributed to greater hydroxide affinity facilitating the deprotonation of surface bound intermediates due to the presence of strong Lewis acidic A-site Bi^{3+} ions. In addition, no amorphization or compositional change was observed for the surface of the fully oxidized $Bi_{0.2}Sr_{0.8}CoO_{3-\delta}$ after OER, where high structural stability is attributed to the higher Fermi level relative to the O 2p band center of $Bi_{0.2}Sr_{0.8}CoO_{3-\delta}$ than that of $SrCoO_{3-\delta}$ as evidenced by density functional theory (DFT) calculations. This work provides a novel example in the design of highly active oxide catalysts for OER by leveraging the inductive effect.

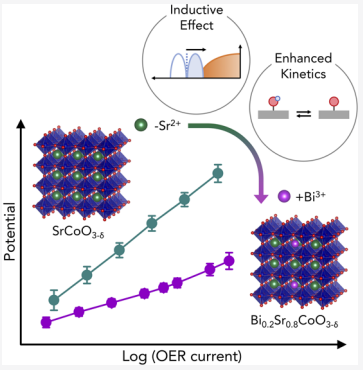

INTRODUCTION

The distribution and on-demand use of electrical energy from sustainable resources, such as solar energy, requires storage technologies that are cost-effective and involve earth-abundant elements. Solar energy can be stored in the form of chemical bonds generated by means of the electrochemical water splitting to produce hydrogen,[1,2] or CO_2 reduction to CO, methanol, and hydrocarbons[3,4] as energy carriers, where oxygen evolution reaction (OER) is required to accompany the above cathodic transformations. These technologies are advantageous to lithium ion batteries for energy storage at scale as they have high gravimetric energy,[5,6] and chemical bonds used for energy storage involve elements (such as O, H, C) that are among the most abundant on the planet. In contrast, energy storage with current Li-ion batteries requires storing each electron using one transition metal ion, and thus, powering the planet with this technology is limited by the availability of metals such as cobalt and nickel in the Earth's crust.[7] The efficiency of the storage technologies based on H_2/CO/CH_3OH/C_nH_{2n+2} production is, however, severely limited to a significant extent by the sluggish reaction kinetics of OER,[8−10] which is catalyzed by precious metal catalysts such as RuO_2[11,12] and IrO_2.[11,13] The development of active OER catalysts composed of earth-abundant elements[14] is therefore crucial for the cost-effective implementation of these technologies.

Late first-row transition metal oxides[15−18] based on cobalt,[19,20] nickel,[21,22] and iron[23,24] are reported to be the most active OER catalysts in basic solution. Experimental and computational studies in the past decade have been focused on elucidating OER mechanisms[8,9] and identifying activity and stability descriptors,[25−27] which can be used to design better catalysts. Perovskites ($ABO_{3-\delta}$) characterized with immense structural, chemical, and electronic flexibility associated with vast selections of A-site and B-site metal ions and oxygen deficiency[28] have been used to develop design principles of OER activity[27,29] and stability.[30,31] Recent works[32,33] have shown that lowering the charge-transfer gap or increasing metal−oxygen covalency in perovskites can improve the OER kinetics, which is faciliated by lowering the energetic barrier of electron transfer for the semiconducting oxides, reducing adsorption strength of oxygenated intermediates of OER[34] or decreasing the energetic barriers[28,32] associated with OER steps on the surface of metallic oxides. Unfortunately, reducing the charge-transfer gap of these perovskites also lowers the Fermi level on the absolute energy scale, placing it below the thermodynamic OER redox potential in the basic solution for the most active catalysts such as $La_{0.5}Sr_{0.5}CoO_{3-\delta}$.[32] This change can generate more negatively charged surface and therefore result in weaker hydroxide affinity (surface reactivity toward hydroxide ions in electrolyte, governed by oxide acidity, Figure S1),[15,35,36] which can impede surface deprotonation

Received: February 18, 2020
Revised: February 25, 2020
Published: February 28, 2020

https://dx.doi.org/10.1021/acs.jpcc.0c01401
J. Phys. Chem. C 2020, 124, 6562−6570

during OER in basic solution (such as $M-OH_{ad} + OH^- \rightarrow M-O_{ad} + H_2O + e^-$).[32] Therefore, tuning the affinity toward hydroxide ions on these highly active oxide surfaces (e.g., by phosphate functionalization)[37] offers new opportunities to further enhance the OER activity.

In this work, we explore the substitution of A-site ions with high electronegativity/Lewis acidity cations in the cobalt perovskites that enables maintenance of high Co−O covalency due to the inductive effect.[38] Introducing the highly Lewis acidic ions can also potentially increase hydroxide affinity on the surface and facilitate OER kinetics, which is supported by the enhanced kinetics previously observed for $LnNiO_3$ perovskite series upon the substitution of La^{3+} with more electronegative Gd^{3+} and Eu^{3+}.[39] Similarly, a strong effect of the A-site electronegativity on the activity of selected perovskites in the hydrogen evolution reaction was also reported.[40] Here, we examine the intrinsic OER activity of bismuth-substituted strontium cobalt perovskites, $Bi_xSr_{1-x}CoO_{3-\delta}$ (x = 0.1, 0.2), where the Bi^{3+} ion possesses one of the highest Lewis acidities (i.e., highest electronegativity) among 2+/3+ A-site ions,[41] with a pK_a value of 1.58, much lower than those of other commonly used A-site metals in cobalt-based perovskite oxides (e.g., $pK_a([Sr^{2+}(H_2O)_n]) = 13.18$, $pK_a([La^{3+}(H_2O)_n]) = 9.06$, $pK_a([Pr^{3+}(H_2O)_n]) = 8.55$). Remarkably, $Bi_{0.2}Sr_{0.8}CoO_{3-\delta}$ that was galvanostatically charged/oxidized to minimize oxygen vacancies exhibits an exceptionally low Tafel slope (~30 mV decade^{-1}) and higher instrinic OER activity than $La_{1-x}Sr_xCoO_{3-\delta}$ and fully oxidized $SrCoO_{3-\delta}$ (one of the most active catalysts reported to date),[34,42] particularly at high current densities (> ~1 mA cm$^{-2}_{oxide}$). The record intrinsic OER activity can be rationalized by stronger affinity toward hydroxide during surface deprotonation associated with more acidic Bi^{3+} than La^{3+} and Sr^{2+}, and comparable Co−O covalency to $SrCoO_{3-\delta}$ as shown from density functional theory (DFT) calculations. In addition, no amorphization or changes in the composition were observed for the surface of fully oxidized $Bi_{0.2}Sr_{0.8}CoO_{3-\delta}$ after OER. Such high structural stability is attributed to the higher Fermi level relative to the O 2p band center of $Bi_{0.2}Sr_{0.8}CoO_{3-\delta}$ than that of $SrCoO_{3-\delta}$. Overall, tuning the electronic structure and surface acid−base chemistry by the rational metal substitution through the inductive effect represents a new strategy for enhancing the activity and stability of OER catalysts.

RESULTS AND DISCUSSION

Synthesis and Characterization of $Bi_{0.2}Sr_{0.8}CoO_{3-\delta}$ at Different Charging States. $Bi_{0.2}Sr_{0.8}CoO_{3-\delta}$ was synthesized through a conventional solid-state route starting from Bi_2O_3, CoO, and $SrCO_3$ precursors[43] as detailed in Supporting Information. Higher levels of bismith subsitution were not explored due to the previously reported solubility limit of ~20%[43] and the necessity to have high Co oxidation state (close to 4+) to achieve high OER activity.[34] Refinement of the powder X-ray diffraction (PXRD) pattern (Figure 1) confirmed a cubic structure with $Pm\bar{3}m$ space group and a unit cell parameter of 3.896 Å (Table S1), which is comparable to that reported in the original study (~3.9 Å).[43] As previous neutron diffraction refinements and cobalt oxidation state (~3) based on iodometric titrations revealed the oxygen vacancy content, $\delta \approx 0.4$, for the as-synthesized $Bi_{0.2}Sr_{0.8}CoO_{3-\delta}$,[43] we estimated $\delta \approx 0.4$ for the oxygen deficiency for our as-synthesized $Bi_{0.2}Sr_{0.8}CoO_{3-\delta}$ sample. This

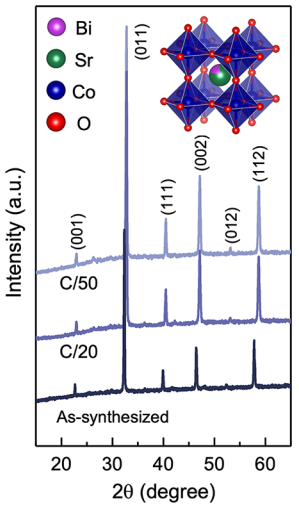

Figure 1. PXRD patterns of as-synthesized oxygen-deficient $Bi_{0.2}Sr_{0.8}CoO_{3-\delta}$ powder, as well as $Bi_{0.2}Sr_{0.8}CoO_{3-\delta}$ galvanostatically charged at 6.1 mA g^{-1} for 20 h (C/20), and at 2.4 mA g^{-1} for 50 h (C/50). Patterns were indexed in a cubic unit cell with space group $Pm\bar{3}m$. All spectra were collected from powder samples (~0.3 g), in a continuous scan mode with a scan rate of 2° per min. The samples were quenched to room temperature after every heat treatment during the solid-state synthesis to minimize the presence of the minor secondary phase of $Bi_2Sr_2Co_3O_y$,[43,50] which could be detected by peaks between 24° and 30° in the PXRD spectra (estimated content <1.7 wt %). Galvanostatic charging experiments were performed for pelletized $Bi_{0.2}Sr_{0.8}CoO_{3-\delta}$ (60 mg, 5 mm in diameter) attached to a graphene sheet (0.120 mm thickness) in O_2-saturated 1 M KOH electrolyte. Inset shows the schematic representation of the crystal structure of $Bi_{0.2}Sr_{0.8}CoO_{3-\delta}$.

assignment is further supported by the Co K-edge X-ray absorption spectroscopy (XAS). The cobalt oxidation state of ~2.96 for as-synthesized $Bi_{0.2}Sr_{0.8}CoO_{3-\delta}$ determined from the position of Co K-edge (Figure S2) is in excellent agreement with the estimated oxygen vacancy level ($\delta \approx 0.4$).

Next, we reduced the oxygen deficiency in $Bi_{0.2}Sr_{0.8}CoO_{3-\delta}$ by slow galvanostatic oxidation/charging (i.e., electrochemical oxygen intercalation) in O_2-saturated 1 M KOH (Figure S3), as higher Co−O bond covalency associated with the presence of Co^{4+} typically imparts higher intrinsic OER activity.[32,34] During galvanostatic charging, two voltage plateaus were observed for thin-film $Bi_{0.2}Sr_{0.8}CoO_{3-\delta}$ deposited on glassy carbon (GC) electrodes, similar to those reported for $La_{0.5}Sr_{0.5}CoO_{3-\delta}$[34] and $SrCoO_{3-\delta}$[34,44] (plateaus are more defined in the latter case, Figure S4), which can be attributed to the filling of oxygen vacancies ($Bi_{0.2}Sr_{0.8}CoO_{3-\delta} + 2\delta OH^- \rightarrow Bi_{0.2}Sr_{0.8}CoO_3 + \delta H_2O + 2\delta e^-$). These two redox events were also observed in the cyclic voltammetry (CV) measurements (Figure 2A) as two redox features centered at ~1.1 V_{RHE} and ~1.4 V_{RHE} on the reversible hydrogen electrode (RHE) scale. Similar redox features reported for other Co-based compounds have been attributed to surface Co^{2+}/Co^{3+} (e.g., $Co^{2+}-H_2O + OH^- \rightarrow Co^{3+}-OH_{ad} + H_2O + e^-$) and Co^{3+}/Co^{4+} (e.g., $Co^{3+}-OH_{ad} + OH^- \rightarrow Co^{4+}-O_{ad} + H_2O + e^-$) redox couples.[20,45,46] The potential of the Co^{3+}/Co^{4+} redox (~1.4 V_{RHE}) before OER was found to decrease with increasing pH (Figure 2B and C), with a pH dependence of ~ −40 mV_{RHE} pH^{-1}. Similar shifts for pre-OER redox features have been found for Ni−Fe oxyhydroxides (up to −60 mV_{RHE} pH^{-1}),[47]

https://dx.doi.org/10.1021/acs.jpcc.0c01401
J. Phys. Chem. C 2020, 124, 6562−6570

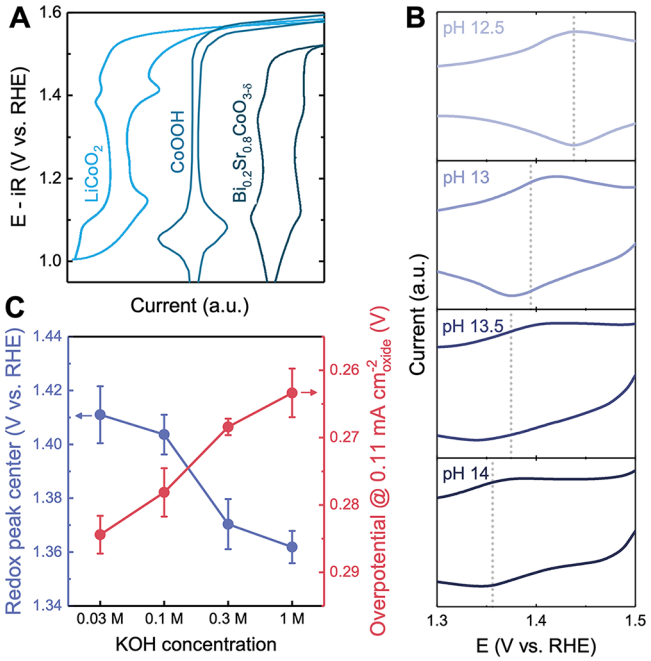

Figure 2. (A) Electrochemical redox behavior of selected Co-based oxides. CV curve of C/50-charged thin-film $Bi_{0.2}Sr_{0.8}CoO_{3-\delta}$ supported on glassy carbon electrode (0.25 mg_{oxide} cm^{-2}_{disk}) compared with previously reported CV curves of $LiCoO_2$[38] (0.1 M) and CoOOH[20] (1 M) in O_2-saturated KOH solutions (scan rate: 10 mV s^{-1}). (B) Representative CV curves for C/50-charged $Bi_{0.2}Sr_{0.8}CoO_{3-\delta}$ electrodes in O_2-saturated KOH with different pHs. Dashed lines show the positions of the redox peak centers. (C) Position of the average redox peak center prior to OER (left, blue) and the OER overpotential (right, red) estimated as the potential required to achieve ~0.11 mA cm^{-2}_{oxide} OER current as assessed from galvanostatic OER measurements for fully oxidized (C/50-charged) $Bi_{0.2}Sr_{0.8}CoO_{3-\delta}$, as a function of the KOH concentration. CV measurements at different KOH concentrations were performed for $Bi_{0.2}Sr_{0.8}CoO_{3-\delta}$ galvanostatically oxidized for 50 h in O_2-saturated 1 M KOH electrolyte with an oxide loading of 0.25 mg_{oxide} cm^{-2}_{disk}.

RuO_2 (101), (001), (001) (up to −27 mV_{RHE} pH^{-1}),[48] and IrO_2 (110) (~−7.5 mV_{RHE} pH^{-1}).[49]

The oxygen intercalation into the bulk structure of $Bi_{0.2}Sr_{0.8}CoO_{3-\delta}$ is supported by the reduction of the unit cell parameter for $Bi_{0.2}Sr_{0.8}CoO_{3-\delta}$ (measured for pelletized samples, without carbon and Nafion binder) after galvanostatic charging as revealed by PXRD analysis (Figure 1), indicative of increased Co oxidation state (i.e., decreased oxygen deficiency level). Oxidized $Bi_{0.2}Sr_{0.8}CoO_{3-\delta}$ samples are characterized with smaller unit cell parameters a = 3.835 Å (C/50 charging rate) and a = 3.838 Å (C/20 charging rate) than as-synthesized $Bi_{0.2}Sr_{0.8}CoO_{3-\delta}$ (a = 3.896 Å). Although the exact value of oxygen deficiency δ on the surface of the galvanostatically oxidized $Bi_{0.2}Sr_{0.8}CoO_{3-\delta}$ is not known, it is proposed that the δ value is close to zero, especially after charging at C/50. This hypothesis is supported by the following observations. First, ~0.8 e^- per formula unit passed before the OER plateau at 1.4 V_{RHE} (Figure S3), which would result in a fully stoichiometric perovskite structure based on the oxygen deficiency level in as-synthesized $Bi_{0.2}Sr_{0.8}CoO_{3-\delta}$ ($\delta \approx 0.4$). Second, as the oxygen intercalation kinetics and oxygen ion transport in peroskites are slow, the surfaces of the oxidized $Bi_{0.2}Sr_{0.8}CoO_{3-\delta}$ can have even smaller δ than the bulk for given charging rates. As the slower galvanostatic charging imparts smaller oxygen deficiency level in $Bi_{0.2}Sr_{0.8}CoO_{3-\delta}$ and other perovskites,[34] we further focused in our work on the OER kinetics of C/50-charged $Bi_{0.2}Sr_{0.8}CoO_{3-\delta}$ (fully oxidized, $\delta \approx 0$).

High Intrinsic OER Activity of the Fully Oxidized (C/50-charged) $Bi_{0.2}Sr_{0.8}CoO_{3-\delta}$ and Its Physical Origin. The OER kinetics of the fully oxidized $Bi_{0.2}Sr_{0.8}CoO_{3-\delta}$ (powder deposited on GC, C/50 charging in O_2-saturated 1 M KOH, Figures S3 and S4) were assessed in O_2-saturated KOH at different pHs through steady-state galvanostatic measurements (Figures S5 and S6), as the contributions of current from electrochemical oxygen intercalation in bulk cannot be excluded completely from the currents obtained by fast CV measurements.[51] The specific OER activity was obtained by normalizing *iR*-corrected kinetic currents to specific oxide surface area from the Brunauer−Emmett−Teller (BET) measurements. The specific OER activity of the galvanostatically oxidized $Bi_{0.2}Sr_{0.8}CoO_{3-\delta}$ is higher than that of other highly active cobalt-based perovskites including oxidized, stoichiometric $La_{0.5}Sr_{0.5}CoO_{3-\delta}$, $Pr_{0.5}Ba_{0.5}CoO_{3-\delta}$, and $SrCoO_{3-\delta}$[34] oxides in O_2-saturated 0.1 M KOH (Figure 3A)

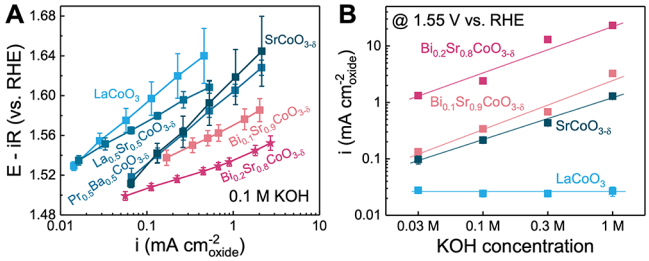

Figure 3. (A) OER intrinsic activity for C/50-charged $Bi_{0.2}Sr_{0.8}CoO_{3-\delta}$, C/50-charged $Bi_{0.1}Sr_{0.9}CoO_{3-\delta}$ and other selected cobalt-based perovskites. Measurements were performed in O_2-saturated 0.1 M KOH electrolyte with an oxide loading of 0.25 mg_{oxide} cm^{-2}_{disk}. Data points were all extracted from steady-state galvanostatic measurements from at least three independent measurements (Figure S6). The OER activity for galvanostatically oxidized $LaCoO_3$, $La_{0.5}Sr_{0.5}CoO_{3-\delta}$, $Pr_{0.5}Ba_{0.5}CoO_{3-\delta}$, and $SrCoO_{3-\delta}$ (having δ close to zero) were taken from galvanostatic measurements in previous work.[34] (B) Specific OER activity of C/50-charged $Bi_{0.2}Sr_{0.8}CoO_{3-\delta}$ and C/50-charged $Bi_{0.1}Sr_{0.9}CoO_{3-\delta}$ at 1.55 V_{RHE} as a function of KOH concentration, with an oxide loading of 0.25 mg_{oxide} cm^{-2}_{disk} on glassy carbon electrode. Data for $Bi_{0.2}Sr_{0.8}CoO_{3-\delta}$ and $Bi_{0.1}Sr_{0.9}CoO_{3-\delta}$ were extracted from OER Tafel plots shown in Figures S12 and S13. Data points for $Bi_{0.2}Sr_{0.8}CoO_{3-\delta}$ (0.3 and 1 M KOH) and $Bi_{0.1}Sr_{0.9}CoO_{3-\delta}$ (1 M KOH) were obtained by the extrapolation of linear Tafel regions from galvanostatic measurements to 1.55 V_{RHE}.

as well as $La_{0.2}Sr_{0.8}CoO_{3-\delta}$ reported previously (activities were assessed by CV measurements)[42] (Figure S7) and RuO_2[48] (Figure S8). Additionally, $Bi_{0.2}Sr_{0.8}CoO_{3-\delta}$ features an exceptionally low Tafel slope of ~30 mV $decade^{-1}$, similar to those found for Ni−Fe oxyhydroxides (~30−40 mV $decade^{-1}$).[47,52,53] $Bi_{0.2}Sr_{0.8}CoO_{3-\delta}$ oxidized upon galvanostatic charging demonstrates specific OER activity at 1.55 V_{RHE} one order of magnitude higher than C/50-charged $Bi_{0.1}Sr_{0.9}CoO_{3-\delta}$ (~45 mV $decade^{-1}$ Tafel slope, Figure S9) as well as oxidized (hence fully stoichiometric) $La_{0.5}Sr_{0.5}CoO_{3-\delta}$, $Pr_{0.5}Ba_{0.5}CoO_{3-\delta}$, and $SrCoO_{3-\delta}$ (~60 mV $decade^{-1}$)[34] in both 0.1 and 1 M KOH, as shown in Figures 3 and S10. Upon surveying highly active oxides reported to date[11,27,54−56] (Figure S11), we conclude that oxidized

https://dx.doi.org/10.1021/acs.jpcc.0c01401
J. Phys. Chem. C 2020, 124, 6562−6570

$Bi_{0.2}Sr_{0.8}CoO_{3-\delta}$ exhibits the highest intrinsic OER activity in 0.1 M KOH reported to date.

Interestingly, $Bi_{0.2}Sr_{0.8}CoO_{3-\delta}$ exhibits pH-dependent OER activity on the RHE scale (~15 mV_{RHE} pH^{-1} at ~0.1 mA cm^{-2}_{oxide}, Figure 2C), where the specific activity increases with increasing pH (Figures 3B and S12−S14). Similar pH-dependent OER activity has been reported for other highly active Co-based oxides including $SrCoO_{3-\delta}$,[34] while less active $LaCoO_3$ exhibits pH-independent OER activity on the RHE scale.[34] A possible OER mechanism responsible for the pH-dependent kinetics of the oxidized $Bi_{0.2}Sr_{0.8}CoO_{3-\delta}$ on the RHE scale will be discussed in later sections.

The high OER activity of C/50-charged ($\delta \approx 0$) $Bi_{0.2}Sr_{0.8}CoO_{3-\delta}$ can be explained by its unique electronic structure, i.e., the retained high cobalt−oxygen covalency after the bismuth substitution. The inductive effect introduced by substituting La^{3+} ions in $La_xSr_{1-x}CoO_{3-\delta}$ with strongly Lewis acidic Bi^{3+} (pK_a for $[Bi(H_2O)_n]^{3+}$ ions is 1.58)[41] in $Bi_{0.2}Sr_{0.8}CoO_{3-\delta}$ could pull more electron density from cobalt ions and lower the energy level of cobalt 3d states (i.e., antibonding cobalt−oxygen orbitals). Therefore, fully oxidized $Bi_{0.2}Sr_{0.8}CoO_{3-\delta}$ has cobalt−oxygen covalency greater than $La_{0.2}Sr_{0.8}CoO_{3-\delta}$ and comparable to $SrCoO_{3-\delta}$ (all featuring δ close to zero), as shown in Figure 4A. This argument is supported by our computed projected density of states (PDOS) for stoichiometric cobalt perovskites, including $Bi_{0.125}Sr_{0.875}CoO_3$ and $Bi_{0.25}Sr_{0.75}CoO_3$ (Figure S15). The energy difference between the cobalt 3d band center and the oxygen 2p band center was used as a measure of the covalency for the cobalt−oxygen bonds, which is fundamentally different from the oxygen p band center position relative to the Fermi level.[32,57] Interestingly, $Bi_{0.25}Sr_{0.75}CoO_3$ was found to have comparable cobalt−oxygen covalency to $SrCoO_3$ but lower oxygen p band center relative to the Fermi level, while having greater covalency than $La_{0.25}Sr_{0.75}CoO_3$ with comparable oxygen p band center relative to the Fermi level, as shown in Figure 4B. Notably, increasing cobalt−oxygen covalency from $LaCoO_3$ and $La_{0.5}Sr_{0.5}CoO_3$ to $Bi_xSr_{1-x}CoO_3$ (x = 0.25, 0.125, and 0) was found to correlate better with increasing OER activity of these oxides than the oxygen p band center relative to the Fermi level.

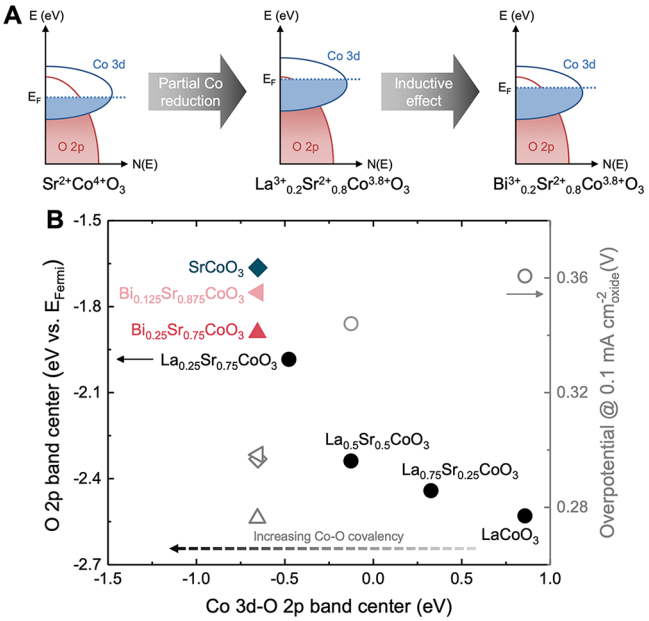

Figure 4. (A) Schematic illustration of the changes in electronic structures upon bismuth substitution from fully stoichiometric $SrCoO_{3-\delta}$ to $Bi_{0.2}Sr_{0.8}CoO_{3-\delta}$ (both having $\delta \approx 0$). (B) Difference between the Co 3d band center and the O 2p band center versus the O 2p band center relative to the Fermi level (left, filled dots) for different stoichiometric cobalt-based perovskites computed at DFT + U level and the experimental OER overpotential (right, open dots) required to achieve ~0.1 mA cm^{-2}_{oxide} OER current in 0.1 M KOH from galvanostatic OER measurements (Figure 3A). $Bi_{0.25}Sr_{0.75}CoO_3$ and $Bi_{0.125}Sr_{0.875}CoO_3$ were used as the simulated compositions for C/50-charged $Bi_{0.2}Sr_{0.8}CoO_{3-\delta}$ and $Bi_{0.1}Sr_{0.9}CoO_{3-\delta}$, respectively. Both the oxygen 2p band and cobalt 3d band centers were determined by taking the centroid of the PDOS of O 2p and cobalt 3d states (Figure S15, both occupied and unoccupied states) relative to the Fermi level. The band centers of $LaCoO_3$, $La_{0.5}Sr_{0.5}CoO_3$, and $Pr_{0.5}Ba_{0.5}CoO_3$ have been reported in previous work.[34] The band centers of $La_{0.75}Sr_{0.25}CoO_3$ have also been reported in previous work.[57]

Maintaining high metal−oxygen covalency (i.e., low charge-transfer gap) in galvanostatically oxidized ($\delta \approx 0$) $Bi_{0.2}Sr_{0.8}CoO_{3-\delta}$ is a key to promote OER kinetics,[32] which can be supported by the computed free energy diagrams of coupled proton−electron transfer OER steps[34] on the cobalt (Figure 5A) and oxygen sites (Figure 5C) of the (001) CoO_2-terminated surfaces of stoichiometric $Bi_{0.25}Sr_{0.75}CoO_3$ and $SrCoO_3$. $SrCoO_3$ was used for comparison here, as it was shown to have the most active cobalt[8,9,57] and oxygen sites[34] in $La_{1-x}Sr_xCoO_3$ series for OER. The free energies of OER intermediates on surface cobalt and oxygen sites are plotted at the lowest potentials needed for all OER steps becoming thermodynamically favorable (Figure 5B and D). The deprotonation of surface hydroxide on cobalt sites (step 1 in Figure 5A, $Co{-}OH_{ad} + OH^- \rightarrow Co{-}O_{ad} + H_2O + e^-$) was found limiting among the four thermodynamic barriers examined for both $SrCoO_3$ and $Bi_{0.25}Sr_{0.75}CoO_3$. The thermodynamically limiting steps for $Bi_{0.25}Sr_{0.75}CoO_3$ might also include the O−O bond formation (step 2 in Figure 5A, $Co{-}O_{ad} + OH^- \rightarrow Co{-}OOH_{ad} + e^-$) because the free energy barriers for $Bi_{0.25}Sr_{0.75}CoO_3$ for these two steps are comparable (with energy difference of ~0.04 eV). The cobalt sites of $Bi_{0.25}Sr_{0.75}CoO_3$ were found to be more active than those of $SrCoO_3$, as the minimum overpotential to make all OER steps thermodynamically favorable was ~0.11 V lower for $Bi_{0.25}Sr_{0.75}CoO_3$. On the other hand, the oxygen sites of $Bi_{0.25}Sr_{0.75}CoO_3$ were comparable to or slightly less active (~0.03 V) than those of $SrCoO_3$. Therefore, assuming an OER pathway with coupled proton−electron transfer, the higher OER activity of oxidized $Bi_{0.2}Sr_{0.8}CoO_{3-\delta}$ compared to $SrCoO_{3-\delta}$ is due to a reduced thermodynamic barrier for the deprotonation of surface hydroxide ($Co{-}OH_{ad} + OH^- \rightarrow Co{-}O_{ad} + H_2O + e^-$) on the surface cobalt sites.

The conventional OER mechanism involving coupled proton−electron transfer in Figure 5 cannot explain the exceptionally low Tafel slope (~30 mV $decade^{-1}$ in 0.1 M KOH) of the oxidized $Bi_{0.2}Sr_{0.8}CoO_{3-\delta}$ as compared to other cobalt-based perovskites (~60 mV $decade^{-1}$), the pH-dependent OER activity (Figures 3B and S12), and the pH-dependent redox peak shift prior to OER (Figure 2B and C). Previous studies have rationalized the pH-dependence on the RHE scale by pathways involving acid−base equilibrium before the rate-limiting step,[58] rate-limiting proton transfer decoupled from electron transfer,[32,34,47,59] and/or electrochemical surface depronationation with noninteger electron transfer.[47,60−62] For instance, for Ni−Fe oxyhydroxides, the observed pH-

https://dx.doi.org/10.1021/acs.jpcc.0c01401
J. Phys. Chem. C 2020, 124, 6562−6570

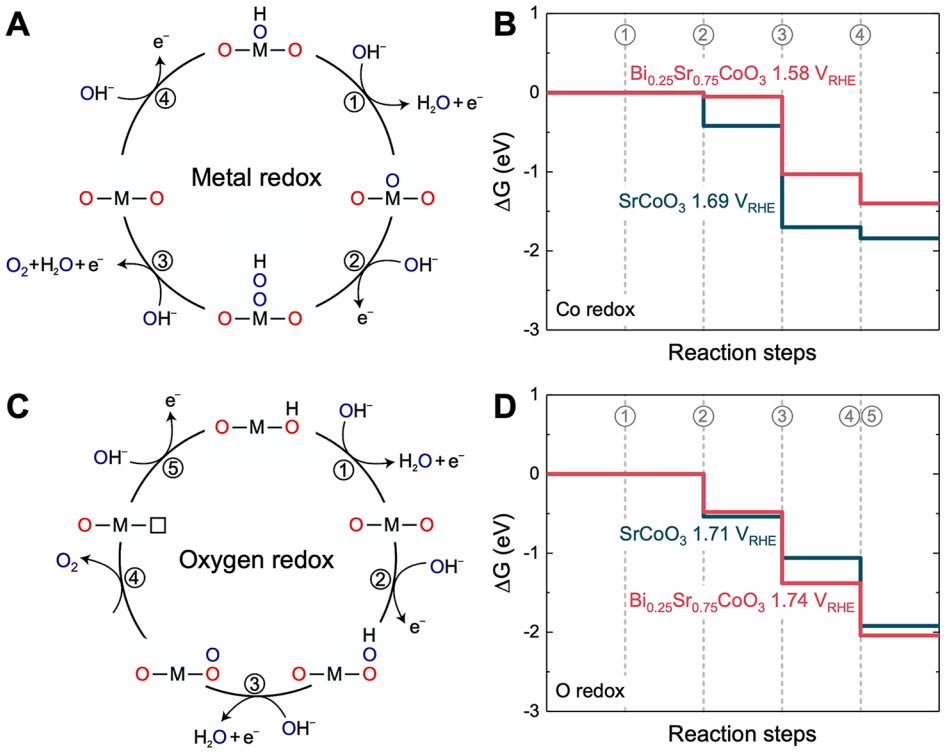

Figure 5. Computed free energy diagrams of coupled proton−electron transfer OER steps on the surface (A, B) cobalt and (C, D) oxygen sites following the OER mechanism proposed in our previous work[10] for the (001) CoO_2-terminated surfaces of stoichiometric $SrCoO_3$ and $Bi_{0.25}Sr_{0.75}CoO_3$ perovskites. The free energies of OER intermediates for each perovskite are plotted at the lowest potential needed for all OER steps becoming thermodynamically downhill.

dependence has been attributed to the nonconcerted metal oxidation coupled with surface hydroxide deprotonation leading to formation of negatively charged intermediates ($NiFe(OH)(OH) + 2OH^- \rightarrow NiFe(O)(O)^- + 2H_2O + e^-$).[47] As highly covalent oxides such as $SrCoO_{3-\delta}$ have Fermi levels below the OER redox potential and are thus characterized by the negatively charged oxide surfaces and reduced hydroxide affinity, oxidized $Bi_{0.2}Sr_{0.8}CoO_{3-\delta}$ was estimated to possess less negatively charged surface and enhanced affinity to hydroxide ions than oxidized $SrCoO_{3-\delta}$ due to the partial reduction of cobalt ions and the upshift of Fermi level after the bismuth substitution (Figures 4, S1 and S16). Moreover, the presence of highly Lewis acidic surface Bi^{3+} ions can potentially increase the ionicity (hence acidity) of the surface O−H bonds (i.e., destabilizing surface intermediates) and facilitate the kinetics of the deprotonation of the surface reaction intermediates during OER.

Here, we propose a possible mechanism to explain the exceptionally low Tafel slope and the pH-dependent OER activity on the RHE scale for oxidized $Bi_{0.2}Sr_{0.8}CoO_{3-\delta}$ (Figure 6). With quasi-equilibrium approximations for reaction steps before the rate-determining step (RDS), the Tafel slope for multistep electrochemical reactions can be given by $60/\alpha$ mV decade^{-1}, where α, the transfer coefficient, can be given by $\alpha = \frac{n_f}{\nu} + n_r\beta$,[63,64] with n_f as the number of electrons transferred before the RDS in the potential range of Tafel analysis, ν as the number of times the RDS occurs for one repetition of the overall OER cycle (=1), n_r as the number of electrons transferred in each occurrence of the RDS (=1 for electrochemical step and = 0 for chemcial step), and β as the symmetry factor (=0.5 for OER).[64] The presence of two pre-

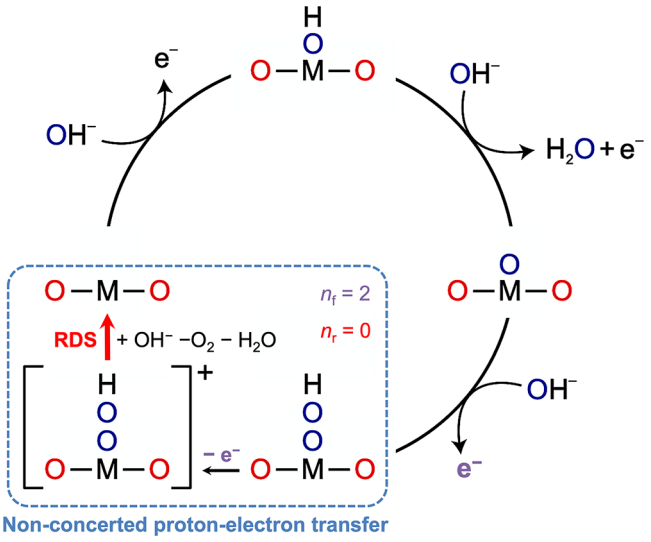

Figure 6. Proposed OER mechanism involving nonconcerted proton−electron transfer for C/50-charged $Bi_{0.2}Sr_{0.8}CoO_{3-\delta}$. n_f and n_r indicate the number of electrons transferred before the RDS in the potential range of Tafel analysis and the number of electrons transferred in each occurrence of the RDS, respectively.

OER redox features (i.e., Co−H_2O to Co−OH_{ad} and Co−OH_{ad} to Co−O_{ad}) for oxidized $Bi_{0.2}Sr_{0.8}CoO_{3-\delta}$ indicates than the oxide surface is O_{ad}-covered before the onset of OER. If we assume the RDS for $Bi_{0.2}Sr_{0.8}CoO_{3-\delta}$ is the final chemical deprotonation step (n_r = 0, e.g., $(Co{-}OOH)^+_{ad} + OH^- \rightarrow Co{-}H_2O + O_2$) and the overall reaction before the RDS transfers two electrons (n_f = 2, e.g. $Co{-}O_{ad} + OH^- \rightarrow$ Co−

https://dx.doi.org/10.1021/acs.jpcc.0c01401
J. Phys. Chem. C 2020, 124, 6562−6570

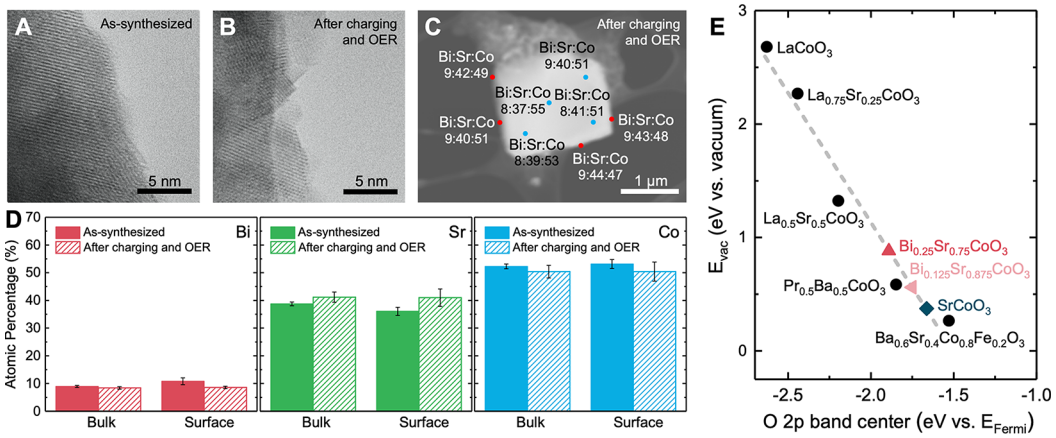

Figure 7. HRTEM images of (A) as-synthesized oxygen-deficient $Bi_{0.2}Sr_{0.8}CoO_{3-\delta}$ powder and (B) C/50-charged $Bi_{0.2}Sr_{0.8}CoO_{3-\delta}$ followed by OER measurments. Galvanostatic charging were performed for oxides films containing Nafion and acetylene black carbon supported on a glassy carbon electrode at 2.4 mA g^{-1} for 50 h in O_2-saturated 1 M KOH electrolyte with an oxide loading of 0.25 mg_{oxide} cm^{-2}_{disk}. (C) Representative high-angular annular dark-field scanning transmission electron microscopy (HAADF-STEM) imaging and corresponding EDX analysis of C/50 fully charged and cycled $Bi_{0.2}Sr_{0.8}CoO_{3-\delta}$. Quantification of the EDX results is shown on the HAADF images. More EDX results for both as-synthesized $Bi_{0.2}Sr_{0.8}CoO_{3-\delta}$ and also fully oxidized and cycled $Bi_{0.2}Sr_{0.8}CoO_{3-\delta}$ can be found in Figure S18. (D) Average bulk and surface Bi, Sr, and Co metal composition in both as-synthesized $Bi_{0.2}Sr_{0.8}CoO_{3-\delta}$ and also galvanostatically oxidized and cycled $Bi_{0.2}Sr_{0.8}CoO_{3-\delta}$ as determined by EDX. The error bars represent the standard deviation of at least eight spots. (E) Computed bulk oxygen vacancy formation energy (E_{vac} vs vacuum, relative to O_2) compared to the computed oxygen 2p band center relative to the Fermi level for $LaCoO_3$, $La_{0.75}Sr_{0.25}CoO_3$, $La_{0.5}Sr_{0.5}CoO_3$, $Pr_{0.5}Ba_{0.5}CoO_3$, $SrCoO_3$, and $Ba_{0.6}Sr_{0.4}Co_{0.2}Fe_{0.8}O_3$ with full oxygen stoichiometry, showing the nearly linear correlation between oxygen vacancy formation energetics and the oxygen 2p band center relative to the Fermi level. This trend can be rationalized by the energetics associated with the creation of oxygen vacancies in the perovskite structure (Figure S21). The energetics of $LaCoO_3$, $La_{0.5}Sr_{0.5}CoO_3$, $Pr_{0.5}Ba_{0.5}CoO_3$, $SrCoO_3$ (E_{vac} only), and $Ba_{0.6}Sr_{0.4}Co_{0.2}Fe_{0.8}O_3$ have been reported in previous work.[34] The energetics of $La_{0.75}Sr_{0.25}CoO_3$ have also been reported in previous work.[57] The oxygen vacancy formation energy for fully stoichiometric $Bi_{0.125}Sr_{0.875}CoO_3$ and $Bi_{0.25}Sr_{0.75}CoO_3$ was further projected following the linear correlation and with the computed oxygen 2p band centers of these two compounds.

$OOH_{ad} + e^-$ and $Co{-}OOH_{ad} \rightarrow (Co{-}OOH)^+_{ad} + e^-$), this scheme will lead to a Tafel slope of 30 mV $decade^{-1}$, which is consistent with our experimental observations (Figure 3A). This proposed OER mechanism is supported by previous conclusions[32] that the chemical deprotonation step is likely to be thermodynamically limiting for highly covalent perovskite oxides such as fully oxidized $Bi_{0.2}Sr_{0.8}CoO_{3-\delta}$. Besides, the pH-dependent Co^{3+}/Co^{4+} redox for $Bi_{0.2}Sr_{0.8}CoO_{3-\delta}$ can also be explained by the nonconcerted metal oxidation coupled with surface hydroxide deprotonation (e.g., with noninteger electron transfer), such as $Co{-}OH_{ad} + OH^- \rightarrow (Co{-}O)^{(1-\delta)-}_{ad} + H_2O + \delta e^-$, which can give rise to a pH dependence of $\left(\frac{\partial E}{\partial pH}\right)_{RHE} = -\frac{59(1-\delta)}{\delta}$ mV_{RHE} pH^{-1} and having $\delta \approx 0.6$ will give rise to the observed pH dependence of -40 mV_{RHE} pH^{-1} (Figure 2B). Therefore, increasing pH lowers the energetic barriers for surface deprotonation, including both the nonconcerted pre-OER redox and the chemical deprotonation RDS for OER (Figures 2C and S17). Further mechanistic studies are required to provide detailed insights on reaction intermediates, e.g., via in situ diffraction[65] and spectroscopic[66] measurements, in order to verify the proposed OER scheme with nonconcerted proton–electron transfer.

Surface Stability under OER Conditions. We have performed high-resolution transmission electron microscopy (HRTEM) imaging and energy-dispersive X-ray (EDX) elemental analysis (Figures 7 and S18) of $Bi_{0.2}Sr_{0.8}CoO_{3-\delta}$ before and after galvanostatic charging (to ~1.4 V_{RHE} at C/50, Figure S4) and OER measurements. No surface amorphization of the oxidized $Bi_{0.2}Sr_{0.8}CoO_{3-\delta}$ after OER was detected from HRTEM analysis (Figure 7B), Raman spectrsocopy (Figure S19), and O K-edge XAS spectroscopy (Figure S20), where the surface remained crystalline like the as-synthesized $Bi_{0.2}Sr_{0.8}CoO_{3-\delta}$ material (Figure 7A). Such high surface stability of the oxidized $Bi_{0.2}Sr_{0.8}CoO_{3-\delta}$ after OER is in contrast to the rapid surface amorphization and the formation of surface hydroxides found for $Ba_{0.5}Sr_{0.5}Co_{0.8}Fe_{0.2}O_{3-\delta}$ and $SrCo_{0.8}Fe_{0.2}O_{3-\delta}$ at OER potentials.[67] In addition, $Bi_{0.2}Sr_{0.8}CoO_{3-\delta}$ appeared to be more stable than $SrCoO_{3-\delta}$, as a few nanometers of amorphous layers were detected on the surface of $SrCoO_{3-\delta}$ particles after OER meaurements.[68] EDX elemental analysis (Figures 7C,D and S18) additionally confirmed no A-site or B-site metal loss after OER, in contrast to the notable A-site metal leaching found in $Ba_{0.5}Sr_{0.5}Co_{0.8}Fe_{0.2}O_{3-\delta}$, $SrCo_{0.8}Fe_{0.2}O_{3-\delta}$, and $Sr_xCa_{1-x}FeO_{3-\delta}$ (x = 0, 0.5 or 1).[67,68] Both bulk and surface metal ratios between A-site (Bi and Sr) and B-site (Co) metals of $Bi_{0.2}Sr_{0.8}CoO_{3-\delta}$ before and after charging and OER measurements were found to be close to 1:4:5 as expected from the nominal stoichiometry.

The high surface stability of $Bi_{0.2}Sr_{0.8}CoO_{3-\delta}$ at OER potentials can be attributed to its lowered O 2p band center with respect to the Fermi level (Figure 7E) in comparison to other highly active Co-based and Fe-based perovskites (such as $SrCoO_{3-\delta}$ and $Ba_{0.5}Sr_{0.5}Co_{0.8}Fe_{0.2}O_{3-\delta}$). The computed oxygen 2p band centers of $Bi_{0.125}Sr_{0.875}CoO_3$ and $Bi_{0.25}Sr_{0.75}CoO_3$ were moved down by ~0.10 eV and ~0.25 eV relative to the Fermi level when compared to stoichiometric $SrCoO_3$, respectively, because the reduction of the nominal cobalt oxidation state (i.e., from +4 in $SrCoO_3$ to +3.875 in $Bi_{0.125}Sr_{0.875}CoO_3$ and +3.75 in $Bi_{0.25}Sr_{0.75}CoO_3$) increases cobalt 3d band filling and upshifts the Fermi level (Figure 4A). Given that the O 2p band center relative to the Fermi level correlates with the formation enthalpy of bulk oxygen vacancies in perovskite oxides (Figures

https://dx.doi.org/10.1021/acs.jpcc.0c01401
J. Phys. Chem. C 2020, 124, 6562–6570

7E and S21), lower O 2p band center of $Bi_{0.2}Sr_{0.8}CoO_{3-\delta}$ relative to the Fermi level imparts higher energy penalty for the creation of oxygen vacancies in the oxide structure compared to $SrCoO_{3-\delta}$, therefore indicative of greater structural stability. The higher surface stability of $Bi_{0.2}Sr_{0.8}CoO_{3-\delta}$ than that of $SrCoO_{3-\delta}$ can be additionally verified by the computed formation enthalpy of surface oxygen vacancies on (001) CoO_2-terminated surfaces of stoichiometric $SrCoO_3$ and $Bi_{0.25}Sr_{0.75}CoO_3$ (Figure S22). The energetic barrier for the creation of surface oxygen vacancies in $SrCoO_3$ is ∼0.75 eV lower than that of $Bi_{0.25}Sr_{0.75}CoO_3$. The trends in formation enthalpy of surface oxygen vacancies are consistent with the energetics of bulk oxygen vacancies (Figure 7E), as well as our experimental observations of the high structural stability (Figures 7 and S18−S20).

CONCLUSIONS

In this study, we report the record intrinsic OER activity and high surface stability of the fully oxidized $Bi_{0.2}Sr_{0.8}CoO_{3-\delta}$ ($\delta \approx 0$) perovskite oxide in alkaline electrolyte. We show that the inductive effect associated with bismuth substitution results in marked increase of the intrinsic OER catalytic activity, exceeding those of other perovskite oxides reported to date. Although Sr^{2+} to Bi^{3+} subtitution reduces the cobalt oxidation state and thus lowers the oxygen 2p band relative to the Fermi level, DFT computations show that high Co−O covalency is maintained, due to the inductive effect from Bi^{3+}, and is comparable with fully stoichiometric $SrCoO_{3-\delta}$ ($\delta = 0$). As the OER kinetics of highly covalent oxides is limited by the deprotonation at the oxide surface, the high OER activity of $Bi_{0.2}Sr_{0.8}CoO_{3-\delta}$ catalyst can be attributed to the enhanced affinity toward hydroxide ions due to the presence of strongly Lewis acidic A-site Bi^{3+} ions on the surface. In addition, the observed pH dependence of the pre-OER redox features and OER activity on the RHE scale implies nonconcerted proton−electron transfer pathways and pH-dependent energetics of intermediate steps. Neither structural nor compositional changes have been found for $Bi_{0.2}Sr_{0.8}CoO_{3-\delta}$ after galvanostatic charging and OER. High surface stability can be attributed to the higher energy penalty for the creation of oxygen vacancies due to the lower oxygen 2p band relative to the Fermi level. By demonstrating how leveraging the inductive effect associated with metal substitution enhances the specific activity of highly OER-active cobalt-based perovskites through maintaining high metal−oxygen covalency and strengthening hydroxide affinity without the expense of surface stability, this work highlights new prospects for the design of novel catalysts for electrochemical energy coversion and storage.

ASSOCIATED CONTENT

Supporting Information

The Supporting Information is available free of charge at https://pubs.acs.org/doi/10.1021/acs.jpcc.0c01401.

Experimental procedures, XAS data, additional electrochemical measurements, DFT calculations, XRD, TEM, EDX, and Raman data (PDF)

AUTHOR INFORMATION

Corresponding Author

Yang Shao-Horn − *Research Laboratory of Electronics, Electrochemical Energy Laboratory, Department of Materials Science and Engineering, and Department of Mechanical Engineering, Massachusetts Institute of Technology, Cambridge, Massachusetts 02139, United States;* orcid.org/0000-0001-8714-2121; Email: shaohorn@mit.edu

Authors

Denis A. Kuznetsov − *Research Laboratory of Electronics and Electrochemical Energy Laboratory, Massachusetts Institute of Technology, Cambridge, Massachusetts 02139, United States;* orcid.org/0000-0002-6925-2367

Jiayu Peng − *Electrochemical Energy Laboratory and Department of Materials Science and Engineering, Massachusetts Institute of Technology, Cambridge, Massachusetts 02139, United States*

Livia Giordano − *Research Laboratory of Electronics, Electrochemical Energy Laboratory, and Department of Mechanical Engineering, Massachusetts Institute of Technology, Cambridge, Massachusetts 02139, United States; Dipartimento di Scienza dei Materiali, Università di Milano-Bicocca, Milano 20126, Italy;* orcid.org/0000-0002-6879-9424

Yuriy Román-Leshkov − *Department of Chemical Engineering, Massachusetts Institute of Technology, Cambridge, Massachusetts 02139, United States;* orcid.org/0000-0002-0025-4233

Complete contact information is available at: https://pubs.acs.org/10.1021/acs.jpcc.0c01401

Author Contributions

#D.A.K. and Y.S.-H. conceived of the project. D.A.K., Y.S.-H., and J.P. designed the experiments. D.A.K. carried out the synthesis and structural characterization. D.A.K. and J.P. performed the electrochemical measurements. J.P. performed the TEM analysis. J.P. and L.G. carried out the DFT calculations. D.A.K. and J.P. prepared the initial draft. All authors contributed to the discussions and revisions of the manuscript. D.A.K. and J. P. contributed equally.

Funding

This work was supported by the Toyota Research Institute through the Accelerated Materials Design and Discovery program. This research used resources of the National Energy Research Scientific Computing Center, a DOE Office of Science User Facility supported by the Office of Science of the U.S. Department of Energy under Contract No. DE-AC02−05CH11231. This work also used resources of the Extreme Science and Engineering Discovery Environment (XSEDE),[69] which is supported by National Science Foundation grant number ACI-1548562. This work made use of the MRSEC Shared Experimental Facilities at MIT, supported by the National Science Foundation under award number DMR-1419807. Part of the research was performed at the Canadian Light Source, a national research facility of the University of Saskatchewan, which is supported by the Canada Foundation for Innovation (CFI), the Natural Sciences and Engineering Research Council (NSERC), the National Research Council (NRC), the Canadian Institutes of Health Research (CIHR), the Government of Saskatchewan, and the University of Saskatchewan. Use of the Stanford Synchrotron Radiation Lightsource, SLAC National Accelerator Laboratory, is supported by the U.S. Department of Energy, Office of Science, Office of Basic Energy Sciences under Contract No. DE-AC02−76SF00515.

Notes

The authors declare no competing financial interest.

■ ACKNOWLEDGMENTS

The authors are grateful to Dr. Juan Corchado Garcia and Dr. Jonathan Hwang for performing O K-edge XAS measurements and data analysis, and to Yang Yu and Dr. Pinar Karayaylali for performing Co K-edge XAS measurements and data analysis.

■ REFERENCES

(1) Seh, Z. W.; Kibsgaard, J.; Dickens, C. F.; Chorkendorff, I. B.; Norskov, J. K.; Jaramillo, T. F. Combining Theory and Experiment in Electrocatalysis: Insights into Materials Design. *Science* **2017**, *355*, No. eaad4998.

(2) McCrory, C. C. L.; Jung, S.; Ferrer, I. M.; Chatman, S. M.; Peters, J. C.; Jaramillo, T. F. Benchmarking Hydrogen Evolving Reaction and Oxygen Evolving Reaction Electrocatalysts for Solar Water Splitting Devices. *J. Am. Chem. Soc.* **2015**, *137*, 4347−4357.

(3) Montoya, J. H.; Seitz, L. C.; Chakthranont, P.; Vojvodic, A.; Jaramillo, T. F.; Norskov, J. K. Materials for Solar Fuels and Chemicals. *Nat. Mater.* **2017**, *16*, 70−81.

(4) Morales-Guio, C. G.; Cave, E. R.; Nitopi, S. A.; Feaster, J. T.; Wang, L.; Kuhl, K. P.; Jackson, A.; Johnson, N. C.; Abram, D. N.; Hatsukade, T.; Hahn, C.; Jaramillo, T. F. Improved CO_2 Reduction Activity towards C_{2+} Alcohols on a Tandem Gold on Copper Electrocatalyst. *Nat. Catal.* **2018**, *1*, 764−771.

(5) Dunn, B.; Kamath, H.; Tarascon, J.-M. Electrical Energy Storage for the Grid: A Battery of Choices. *Science* **2011**, *334*, 928−935.

(6) Goodenough, J. B.; Park, K.-S. The Li-Ion Rechargeable Battery: A Perspective. *J. Am. Chem. Soc.* **2013**, *135*, 1167−1176.

(7) Turcheniuk, K.; Bondarev, D.; Singhal, V.; Yushin, G. Ten Years Left to Redesign Lithium-Ion Batteries. *Nature* **2018**, *559*, 467−470.

(8) Rossmeisl, J.; Qu, Z. W.; Zhu, H.; Kroes, G. J.; Norskov, J. K. Electrolysis of Water on Oxide Surfaces. *J. Electroanal. Chem.* **2007**, *607*, 83−89.

(9) Man, I. C.; Su, H.-Y.; Calle-Vallejo, F.; Hansen, H. A.; Martinez, J. I.; Inoglu, N. G.; Kitchin, J.; Jaramillo, T. F.; Norskov, J. K.; Rossmeisl, J. Universality in Oxygen Evolution Electrocatalysis on Oxide Surfaces. *ChemCatChem* **2011**, *3*, 1159−1165.

(10) Dau, H.; Limberg, C.; Reier, T.; Risch, M.; Roggan, S.; Strasser, P. The Mechanism of Water Oxidation: From Electrolysis via Homogeneous to Biological Catalysis. *ChemCatChem* **2010**, *2*, 724−761.

(11) Lee, Y.; Suntivich, J.; May, K. J.; Perry, E. E.; Shao-Horn, Y. Synthesis and Activities of Rutile IrO_2 and RuO_2 Nanoparticles for Oxygen Evolution in Acid and Alkaline Solutions. *J. Phys. Chem. Lett.* **2012**, *3*, 399−404.

(12) Fang, Y.-H.; Liu, Z.-P. Mechanism and Tafel Lines of Electro-Oxidation of Water to Oxygen on RuO_2(110). *J. Am. Chem. Soc.* **2010**, *132*, 18214−18222.

(13) Sanchez Casalongue, H. G.; Ng, M. L.; Kaya, S.; Friebel, D.; Ogasawara, H.; Nilsson, A. In Situ Observation of Surface Species on Iridium Oxide Nanoparticles during the Oxygen Evolution Reaction. *Angew. Chem., Int. Ed.* **2014**, *53*, 7169−7172.

(14) Du, P.; Eisenberg, R. Catalysts Made of Earth-Abundant Elements (Co, Ni, Fe) for Water Splitting: Recent Progress and Future Challenges. *Energy Environ. Sci.* **2012**, *5*, 6012−6021.

(15) Bockris, J. O. M.; Otagawa, T. The Electrocatalysis of Oxygen Evolution on Perovskites. *J. Electrochem. Soc.* **1984**, *131*, 290−302.

(16) Matsumoto, Y.; Sato, E. Electrocatalytic Properties of Transition Metal Oxides for Oxygen Evolution Reaction. *Mater. Chem. Phys.* **1986**, *14*, 397−426.

(17) Wei, C.; Feng, Z. X.; Scherer, G. G.; Barber, J.; Shao-Horn, Y.; Xu, Z. C. J. Cations in Octahedral Sites: A Descriptor for Oxygen Electrocatalysis on Transition-Metal Spinels. *Adv. Mater.* **2017**, *29*, 8.

(18) Burke, M. S.; Enman, L. J.; Batchellor, A. S.; Zou, S.; Boettcher, S. W. Oxygen Evolution Reaction Electrocatalysis on Transition Metal Oxides and (Oxy)hydroxides: Activity Trends and Design Principles. *Chem. Mater.* **2015**, *27*, 7549−7558.

(19) Kanan, M. W.; Nocera, D. G. In Situ Formation of an Oxygen-Evolving Catalyst in Neutral Water Containing Phosphate and Co^{2+}. *Science* **2008**, *321*, 1072−1075.

(20) Burke, M. S.; Kast, M. G.; Trotochaud, L.; Smith, A. M.; Boettcher, S. W. Cobalt-Iron (Oxy)hydroxide Oxygen Evolution Electrocatalysts: The Role of Structure and Composition on Activity, Stability, and Mechanism. *J. Am. Chem. Soc.* **2015**, *137*, 3638−3648.

(21) Dincă, M.; Surendranath, Y.; Nocera, D. G. Nickel-Borate Oxygen-Evolving Catalyst that Functions under Benign Conditions. *Proc. Natl. Acad. Sci. U. S. A.* **2010**, *107*, 10337.

(22) Ng, J. W. D.; García-Melchor, M.; Bajdich, M.; Chakthranont, P.; Kirk, C.; Vojvodic, A.; Jaramillo, T. F. Gold-Supported Cerium-Doped NiO_x Catalysts for Water Oxidation. *Nat. Energy* **2016**, *1*, 16053.

(23) Friebel, D.; Louie, M. W.; Bajdich, M.; Sanwald, K. E.; Cai, Y.; Wise, A. M.; Cheng, M.-J.; Sokaras, D.; Weng, T.-C.; Alonso-Mori, R.; Davis, R. C.; Bargar, J. R.; Norskov, J. K.; Nilsson, A.; Bell, A. T. Identification of Highly Active Fe Sites in (Ni,Fe)OOH for Electrocatalytic Water Splitting. *J. Am. Chem. Soc.* **2015**, *137*, 1305−1313.

(24) Chemelewski, W. D.; Lee, H.-C.; Lin, J.-F.; Bard, A. J.; Mullins, C. B. Amorphous FeOOH Oxygen Evolution Reaction Catalyst for Photoelectrochemical Water Splitting. *J. Am. Chem. Soc.* **2014**, *136*, 2843−2850.

(25) Hong, W. T.; Risch, M.; Stoerzinger, K. A.; Grimaud, A.; Suntivich, J.; Shao-Horn, Y. Toward the Rational Design of Non-Precious Transition Metal Oxides for Oxygen Electrocatalysis. *Energy Environ. Sci.* **2015**, *8*, 1404−1427.

(26) Grimaud, A.; May, K. J.; Carlton, C. E.; Lee, Y.-L.; Risch, M.; Hong, W. T.; Zhou, J.; Shao-Horn, Y. Double Perovskites as a Family of Highly Active Catalysts for Oxygen Evolution in Alkaline Solution. *Nat. Commun.* **2013**, *4*, 2439.

(27) Suntivich, J.; May, K. J.; Gasteiger, H. A.; Goodenough, J. B.; Shao-Horn, Y. A Perovskite Oxide Optimized for Oxygen Evolution Catalysis from Molecular Orbital Principles. *Science* **2011**, *334*, 1383−1385.

(28) Hwang, J.; Rao, R. R.; Giordano, L.; Katayama, Y.; Yu, Y.; Shao-Horn, Y. Perovskites in Catalysis and Electrocatalysis. *Science* **2017**, *358*, 751−756.

(29) Jacobs, R.; Hwang, J.; Shao-Horn, Y.; Morgan, D. Assessing Correlations of Perovskite Catalytic Performance with Electronic Structure Descriptors. *Chem. Mater.* **2019**, *31*, 785−797.

(30) Grimaud, A.; Demortiere, A.; Saubanere, M.; Dachraoui, W.; Duchamp, M.; Doublet, M.-L.; Tarascon, J.-M. Activation of Surface Oxygen Sites on an Iridium-Based Model Catalyst for the Oxygen Evolution Reaction. *Nat. Energy* **2017**, *2*, 16189.

(31) Kim, Y.-T.; Lopes, P. P.; Park, S.-A.; Lee, A. Y.; Lim, J.; Lee, H.; Back, S.; Jung, Y.; Danilovic, N.; Stamenkovic, V.; Erlebacher, J.; Snyder, J.; Markovic, N. M. Balancing Activity, Stability and Conductivity of Nanoporous Core-Shell Iridium/Iridium Oxide Oxygen Evolution Catalysts. *Nat. Commun.* **2017**, *8*, 1449.

(32) Hong, W. T.; Stoerzinger, K. A.; Lee, Y.-L.; Giordano, L.; Grimaud, A.; Johnson, A. M.; Hwang, J.; Crumlin, E. J.; Yang, W.; Shao-Horn, Y. Charge-Transfer-Energy-Dependent Oxygen Evolution Reaction Mechanisms for Perovskite Oxides. *Energy Environ. Sci.* **2017**, *10*, 2190−2200.

(33) Yamada, I.; Takamatsu, A.; Asai, K.; Ohzuku, H.; Shirakawa, T.; Uchimura, T.; Kawaguchi, S.; Tsukasaki, H.; Mori, S.; Wada, K.; Ikeno, H.; Yagi, S. Synergistically Enhanced Oxygen Evolution Reaction Catalysis for Multielement Transition-Metal Oxides. *ACS Appl. Energy Mater.* **2018**, *1*, 3711−3721.

(34) Grimaud, A.; Diaz-Morales, O.; Han, B. H.; Hong, W. T.; Lee, Y. L.; Giordano, L.; Stoerzinger, K. A.; Koper, M. T. M.; Shao-Horn, Y. Activating Lattice Oxygen Redox Reactions in Metal Oxides to Catalyse Oxygen Evolution. *Nat. Chem.* **2017**, *9*, 457−465.

(35) Portier, J.; Poizot, P.; Campet, G.; Subramanian, M. A.; Tarascon, J. M. Acid−Base Behavior of Oxides and Their Electronic Structure. *Solid State Sci.* **2003**, *5*, 695−699.

https://dx.doi.org/10.1021/acs.jpcc.0c01401
J. Phys. Chem. C 2020, 124, 6562−6570

(36) Matar, S. F.; Campet, G.; Subramanian, M. A. Electronic Properties of Oxides: Chemical and Theoretical Approaches. *Prog. Solid State Chem.* **2011**, *39*, 70−95.
(37) Yang, C.; Laberty-Robert, C.; Batuk, D.; Cibin, G.; Chadwick, A. V.; Pimenta, V.; Yin, W.; Zhang, L.; Tarascon, J.-M.; Grimaud, A. Phosphate Ion Functionalization of Perovskite Surfaces for Enhanced Oxygen Evolution Reaction. *J. Phys. Chem. Lett.* **2017**, *8*, 3466−3472.
(38) Kuznetsov, D. A.; Han, B.; Yu, Y.; Rao, R. R.; Hwang, J.; Roman-Leshkov, Y.; Shao-Horn, Y. Tuning Redox Transitions via Inductive Effect in Metal Oxides and Complexes, and Implications in Oxygen Electrocatalysis. *Joule* **2018**, *2*, 225−244.
(39) Hong, W. T.; Welsch, R. E.; Shao-Horn, Y. Descriptors of Oxygen-Evolution Activity for Oxides: A Statistical Evaluation. *J. Phys. Chem. C* **2016**, *120*, 78−86.
(40) Guan, D.; Zhou, J.; Huang, Y.-C.; Dong, C.-L.; Wang, J.-Q.; Zhou, W.; Shao, Z. Screening Highly Active Perovskites for Hydrogen-Evolving Reaction via Unifying Ionic Electronegativity Descriptor. *Nat. Commun.* **2019**, *10*, 3755.
(41) Dean, J. A.; Lange, N. A. *Lange's Handbook of Chemistry*; McGraw-Hill: 1999.
(42) Mefford, J. T.; Rong, X.; Abakumov, A. M.; Hardin, W. G.; Dai, S.; Kolpak, A. M.; Johnston, K. P.; Stevenson, K. J. Water Electrolysis on $La_{1-x}Sr_xCoO_{3-\delta}$ Perovskite Electrocatalysts. *Nat. Commun.* **2016**, *7*, 11053.
(43) Knee, C. S.; Lindberg, F.; Khan, N.; Svensson, G.; Svedlindh, P.; Rundlöf, H.; Eriksson, S. G.; Börjesson, L. Influence of Oxygen Defects on the Structure and Magnetic Properties of $Sr_{1-x}Bi_xCoO_{3-y}$ ($0.1 \leq x \leq 0.2$) Supercell Perovskites. *Chem. Mater.* **2006**, *18*, 1354−1364.
(44) Nemudry, A.; Rudolf, P.; Schöllhorn, R. Topotactic Electrochemical Redox Reactions of the Defect Perovskite $SrCoO_{2.5+x}$. *Chem. Mater.* **1996**, *8*, 2232−2238.
(45) Mizushima, K.; Jones, P. C.; Wiseman, P. J.; Goodenough, J. B. Li_xCoO_2 ($0 < x < -1$): A New Cathode Material for Batteries of High Energy Density. *Mater. Res. Bull.* **1980**, *15*, 783−789.
(46) Han, B.; Qian, D.; Risch, M.; Chen, H.; Chi, M.; Meng, Y. S.; Shao-Horn, Y. Role of $LiCoO_2$ Surface Terminations in Oxygen Reduction and Evolution Kinetics. *J. Phys. Chem. Lett.* **2015**, *6*, 1357−1362.
(47) Görlin, M.; Ferreira de Araújo, J.; Schmies, H.; Bernsmeier, D.; Dresp, S.; Gliech, M.; Jusys, Z.; Chernev, P.; Kraehnert, R.; Dau, H.; Strasser, P. Tracking Catalyst Redox States and Reaction Dynamics in Ni−Fe Oxyhydroxide Oxygen Evolution Reaction Electrocatalysts: The Role of Catalyst Support and Electrolyte pH. *J. Am. Chem. Soc.* **2017**, *139*, 2070−2082.
(48) Stoerzinger, K. A.; Rao, R. R.; Wang, X. R.; Hong, W. T.; Rouleau, C. M.; Shao-Horn, Y. The Role of Ru Redox in pH-Dependent Oxygen Evolution on Rutile Ruthenium Dioxide Surfaces. *Chem.* **2017**, *2*, 668−675.
(49) Kuo, D.-Y.; Kawasaki, J. K.; Nelson, J. N.; Kloppenburg, J.; Hautier, G.; Shen, K. M.; Schlom, D. G.; Suntivich, J. Influence of Surface Adsorption on the Oxygen Evolution Reaction on $IrO_2(110)$. *J. Am. Chem. Soc.* **2017**, *139*, 3473−3479.
(50) Tarascon, J. M.; Ramesh, R.; Barboux, P.; Hedge, M. S.; Hull, G. W.; Greene, L. H.; Giroud, M.; LePage, Y.; McKinnon, W. R.; Waszcak, J. V.; Schneemeyer, L. F. New Non-Superconducting Layered Bi-oxide Phases of Formula $Bi_2M_3Co_2O_y$ Containing Co instead of Cu. *Solid State Commun.* **1989**, *71*, 663−668.
(51) Wei, C.; Rao, R. R.; Peng, J.; Huang, B.; Stephens, I. E. L.; Risch, M.; Xu, Z. J.; Shao-Horn, Y. Recommended Practices and Benchmark Activity for Hydrogen and Oxygen Electrocatalysis in Water Splitting and Fuel Cells. *Adv. Mater.* **2019**, *31*, 1806296.
(52) Gong, M.; Li, Y.; Wang, H.; Liang, Y.; Wu, J. Z.; Zhou, J.; Wang, J.; Regier, T.; Wei, F.; Dai, H. An Advanced Ni−Fe Layered Double Hydroxide Electrocatalyst for Water Oxidation. *J. Am. Chem. Soc.* **2013**, *135*, 8452−8455.
(53) Burke, M. S.; Zou, S.; Enman, L. J.; Kellon, J. E.; Gabor, C. A.; Pledger, E.; Boettcher, S. W. Revised Oxygen Evolution Reaction Activity Trends for First-Row Transition-Metal (Oxy)hydroxides in Alkaline Media. *J. Phys. Chem. Lett.* **2015**, *6*, 3737−3742.
(54) Yagi, S.; Yamada, I.; Tsukasaki, H.; Seno, A.; Murakami, M.; Fujii, H.; Chen, H.; Umezawa, N.; Abe, H.; Nishiyama, N.; Mori, S. Covalency-Reinforced Oxygen Evolution Reaction Catalyst. *Nat. Commun.* **2015**, *6*, 8249.
(55) Lee, J. G.; Hwang, J.; Hwang, H. J.; Jeon, O. S.; Jang, J.; Kwon, O.; Lee, Y.; Han, B.; Shul, Y.-G. A New Family of Perovskite Catalysts for Oxygen-Evolution Reaction in Alkaline Media: $BaNiO_3$ and $BaNi_{0.83}O_{2.5}$. *J. Am. Chem. Soc.* **2016**, *138*, 3541−3547.
(56) Forslund, R. P.; Hardin, W. G.; Rong, X.; Abakumov, A. M.; Filimonov, D.; Alexander, C. T.; Mefford, J. T.; Iyer, H.; Kolpak, A. M.; Johnston, K. P.; Stevenson, K. J. Exceptional Electrocatalytic Oxygen Evolution via Tunable Charge Transfer Interactions in $La_{0.5}Sr_{1.5}Ni_{1-x}Fe_xO_{4\pm\delta}$ Ruddlesden-Popper Oxides. *Nat. Commun.* **2018**, *9*, 3150.
(57) Lee, Y. L.; Kleis, J.; Rossmeisl, J.; Shao-Horn, Y.; Morgan, D. Prediction of Solid Oxide Fuel Cell Cathode Activity with First-Principles Descriptors. *Energy Environ. Sci.* **2011**, *4*, 3966−3970.
(58) Koper, M. T. M. Theory of the Transition from Sequential to Concerted Electrochemical Proton−Electron Transfer. *Phys. Chem. Chem. Phys.* **2013**, *15*, 1399−1407.
(59) Giordano, L.; Han, B. H.; Risch, M.; Hong, W. T.; Rao, R. R.; Stoerzinger, K. A.; Shao-Horn, Y. pH Dependence of OER Activity of Oxides: Current and Future Perspectives. *Catal. Today* **2016**, *262*, 2−10.
(60) Schwarz, K.; Xu, B.; Yan, Y.; Sundararaman, R. Partial Oxidation of Step-Bound Water Leads to Anomalous pH Effects on Metal Electrode Step-Edges. *Phys. Chem. Chem. Phys.* **2016**, *18*, 16216−16223.
(61) van der Niet, M. J. T. C.; Garcia-Araez, N.; Hernandez, J.; Feliu, J. M.; Koper, M. T. M. Water Dissociation on Well-Defined Platinum Surfaces: The Electrochemical Perspective. *Catal. Today* **2013**, *202*, 105−113.
(62) Gisbert, R.; García, G.; Koper, M. T. M. Adsorption of Phosphate Species on Poly-Oriented Pt and Pt(111) Electrodes over a Wide Range of pH. *Electrochim. Acta* **2010**, *55*, 7961−7968.
(63) Bockris, J. O. M.; Reddy, A. K. N.; Gamboa-Aldeco, M. E. *Modern Electrochemistry 2A: Fundamentals of Electrodics*; Springer: 2000.
(64) Bockris, J. O. M. Kinetics of Activation Controlled Consecutive Electrochemical Reactions: Anodic Evolution of Oxygen. *J. Chem. Phys.* **1956**, *24*, 817−827.
(65) Rao, R. R.; Kolb, M. J.; Halck, N. B.; Pedersen, A. F.; Mehta, A.; You, H.; Stoerzinger, K. A.; Feng, Z. X.; Hansen, H. A.; Zhou, H.; Giordano, L.; Rossmeisl, J.; Vegge, T.; Chorkendorff, I.; Stephens, I. E. L.; Shao-Horn, Y. Towards Identifying the Active Sites on $RuO_2(110)$ in Catalyzing Oxygen Evolution. *Energy Environ. Sci.* **2017**, *10*, 2626−2637.
(66) Katayama, Y.; Nattino, F.; Giordano, L.; Hwang, J.; Rao, R. R.; Andreussi, O.; Marzari, N.; Shao-Horn, Y. An In Situ Surface-Enhanced Infrared Absorption Spectroscopy Study of Electrochemical CO2 Reduction: Selectivity Dependence on Surface C-Bound and O-Bound Reaction Intermediates. *J. Phys. Chem. C* **2019**, *123*, 5951−5963.
(67) May, K. J.; Carlton, C. E.; Stoerzinger, K. A.; Risch, M.; Suntivich, J.; Lee, Y.-L.; Grimaud, A.; Shao-Horn, Y. Influence of Oxygen Evolution during Water Oxidation on the Surface of Perovskite Oxide Catalysts. *J. Phys. Chem. Lett.* **2012**, *3*, 3264−3270.
(68) Han, B. H.; Grimaud, A.; Giordano, L.; Hong, W. T.; Diaz-Morales, O.; Yueh-Lin, L.; Hwang, J.; Charles, N.; Stoerzinger, K. A.; Yang, W. L.; Koper, M. T. M.; Shao-Horn, Y. Iron-Based Perovskites for Catalyzing Oxygen Evolution Reaction. *J. Phys. Chem. C* **2018**, *122*, 8445−8454.
(69) Towns, J.; Cockerill, T.; Dahan, M.; Foster, I.; Gaither, K.; Grimshaw, A.; Hazlewood, V.; Lathrop, S.; Lifka, D.; Peterson, G. D.; Roskies, R.; Scott, J. R.; Wilkins-Diehr, N. XSEDE: Accelerating Scientific Discovery. *Comput. Sci. Eng.* **2014**, *16*, 62−74.

https://dx.doi.org/10.1021/acs.jpcc.0c01401
J. Phys. Chem. C 2020, 124, 6562−6570